Decay rate of magnetic dipoles near nonmagnetic nanostructures

Peter R. Wiecha,* Arnaud Arbouet, Aurélien Cuche, Vincent Paillard, and Christian Girard
CEMES-CNRS, Université de Toulouse, CNRS, UPS, Toulouse, France

(Received 23 July 2017; revised manuscript received 23 January 2018; published 8 February 2018)

In this article, we propose a concise theoretical framework based on mixed-field susceptibilities to describe the decay of magnetic dipoles induced by nonmagnetic nanostructures. This approach is first illustrated in simple cases in which analytical expressions of the decay rate can be obtained. We then show that a more refined numerical implementation of this formalism involving a volume discretization and the computation of a generalized propagator can predict the dynamics of magnetic dipoles in the vicinity of nanostructures of arbitrary geometries. We finally demonstrate the versatility of this numerical method by coupling it to an evolutionary optimization algorithm. In this way we predict a structure geometry which maximally promotes the decay of magnetic transitions with respect to electric emitters.

DOI: 10.1103/PhysRevB.97.085411

I. INTRODUCTION

During the last two decades, the development of nano-optics has provided a wealth of strategies to tailor electric and magnetic fields down to the subwavelength scale [1]. In particular, optical nanoantennas have allowed one to modify the intensity, dynamics, or directionality of light emission from fluorophores placed in the near-field of nano-objects using concepts from the radio-frequency domain [2–8]. These studies have been performed nearly exclusively on fluorophores supporting electric dipole (ED) transitions, the latter being $\sim a_0/\lambda_0 \sim 10^4$–$10^5$ larger than their magnetic dipole (MD) counterpart in the optical frequency range (a_0 being the Bohr radius and λ_0 the transition wavelength) [9]. Recently, delicate experiments have addressed light emission from rare-earth-doped emitters supporting both strong MD and ED transitions [10,11]. Three-dimensional maps of the luminescence of Eu^{3+}-doped nanocrystals scanned in the near field of gold stripes have revealed variations in the relative intensities of ED and MD transitions [10,12]. In these experiments, the fluorescence intensity, photon statistics, and branching ratios are directly related to the decay rates of the ED or MD radiative transitions, the latter being ultimately connected to the electric or magnetic part of the local density of electromagnetic states (EM-LDOS) [10,13–15]. Independently of the nature of the transition, the alteration of the EM-LDOS by a nanostructure arises from the back action of the electric or magnetic field on the transition dipole [2,16–19].

Analytical expressions for the decay of magnetic transitions have been derived for the simple case of single [20–22] or also multiple spheres [18,23]. For more complex geometries or arrangements of nanostructures, standard numerical tools such as the finite difference time domain (FDTD) or finite element method (FEM) can be employed to calculate magnetic decay rates. To do so, a kind of numerical experiment is performed where the radiated power of a dipole emitter is compared for the cases with, and in absence of, a nanostructure [24–28]. Whereas the underlying physics is well understood, a unified description of the dynamics of a fluorophore supporting MD transitions in the presence of nonmagnetic nanostructures of arbitrary shape is still lacking.

The confinement of the magnetic field around nonmagnetic nano-objects arises from the spatial variations of the electric near field in the immediate proximity of a nanostructure. When the surface is illuminated by a plane wave or an evanescent surface wave, both experimental data and numerical simulations reveal spatial modulations in the electric and magnetic near-field intensities. For example, the magnetic field intensity recorded above subwavelength-sized dielectric particles, excited by a *p*-polarized surface wave, has a strong and dark contrast while a completely opposite behavior is observed for the electric field intensity [29–31]. If now the nanostructure is no longer illuminated by a plane wave but by a dipole source, the response fields (electric or magnetic) are different and shape the decay rate and the corresponding dipolar luminescence. From a mathematical point of view, the magnetic near field can be described by a set of mixed-field susceptibilities capable of connecting an electrical polarization, oscillating at an optical frequency ω_0, to a magnetic field vector oscillating at the same frequency [32,33]. In fact, these field susceptibilities are a generalized form of the usual Green's dyadic tensor [34,35]. Historically, they were introduced by Agarwal to describe energy transfers in the presence of dielectric or metallic planar surfaces [36]. Mixed-field susceptibilities can be used to evaluate the optical magnetic near field or the optical response of nanostructures possessing an intrinsic magnetic polarizability, such as metallic rings or split rings [33,37]. In recent works, they have been used to separately study the magnetic and electric part of the LDOS close to a surface [38] and for the calculation of the EM-LDOS in proximity of periodic arrays of magnetoelectric point scatterers [39].

In this article, we first extend Agarwal's theory by presenting an analytical scheme yielding the total decay rate of a MD transition Γ_m in terms of mixed *electric-magnetic* field susceptibilities. From this concise mathematical framework,

*peter.wiecha@cemes.fr

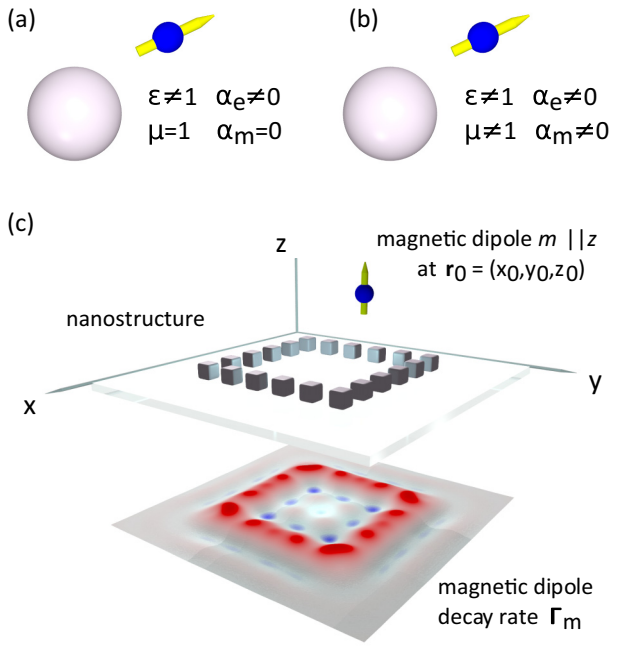

FIG. 1. (a) and (b) Illustration of two possible kinds of optical coupling between an oscillating magnetic dipole and a nanostructure defined by arbitrary optical permittivity $\epsilon(\omega_0)$ and permeability $\mu(\omega_0)$, with α_e and α_m the electric and magnetic polarizabilities. The present study focuses on the first case in which the magnetic dipole is coupled to a nonmagnetic nanostructure, as shown in (a). (c) Decay rate of a magnetic dipole $m(\omega_0)$ oriented along OZ and scanned at $z_0 = 30$ nm above the depicted nanostructure.

we develop a flexible and powerful numerical tool to compute the decay rate of magnetic dipoles near dielectric or metallic nanostructures of arbitrary shapes (see an example in Fig. 1). In a second step, we explore the decay-rate maps generated by the coupling between rare-earth atoms and dielectric nanostructures. We highlight and discuss the differences between electric and magnetic decay-rate topographies. Finally, we demonstrate the versatility of our mathematical framework by coupling it to an evolutionary optimization algorithm to predict a metallic nanostructure yielding an optimum contrast between the magnetic and electric parts of the EM-LDOS.

II. MAGNETIC FIELD SUSCEPTIBILITY FOR NONMAGNETIC STRUCTURES

The two possible kinds of coupling between a magnetic dipole transition and a subwavelength-sized sphere are schematized in Figs. 1(a) and 1(b). The first one is the coupling with a standard material (bulk metal, dielectric, or semiconductor) which does not possess any intrinsic magnetic response [i.e., for which the magnetic permeability is equal to unity (cgs units)] while the second one is the direct magnetic coupling such as the one involved in the presence of artificial *left-handed* materials, i.e., materials with simultaneously negative permeability and permittivity [40,41]. We address exclusively the first situation and therefore assume that $\mu(\omega_0) = 1$ at all wavelengths. We consider the geometry depicted in Fig. 1. The electric and magnetic fields generated at $\mathbf{r}$ by a magnetic dipole $\mathbf{m}(\omega_0)$ located at $\mathbf{r}_0$ are defined by [36]

$$\mathbf{E}_0(\mathbf{r},\omega_0) = ik_0 \nabla_{\mathbf{r}} \wedge \mathcal{G}_0(\mathbf{r},\mathbf{r}_0,\omega_0)\mathbf{m}(\omega_0), \tag{1}$$

and

$$\mathbf{H}_0(\mathbf{r},\omega_0) = \left\{\mathbf{I}k_0^2 + \nabla_{\mathbf{r}}\nabla_{\mathbf{r}}\right\}\mathcal{G}_0(\mathbf{r},\mathbf{r}_0,\omega_0)\cdot\mathbf{m}(\omega_0), \tag{2}$$

where $k_0 = 2\pi/\lambda_0$ is the wave vector in vacuum, $\mathbf{I}$ the identity matrix, and $\mathcal{G}_0 = \exp(ik_0|\mathbf{r}-\mathbf{r}_0|)/|\mathbf{r}-\mathbf{r}_0|$ represents the scalar Green's function. From these two equations, we can define two field susceptibilities,

$$\mathbf{E}_0(\mathbf{r},\omega_0) = \mathcal{S}^{EH}(\mathbf{r},\mathbf{r}_0,\omega_0)\cdot\mathbf{m}(\omega_0), \tag{3}$$

and

$$\mathbf{H}_0(\mathbf{r},\omega_0) = \mathcal{S}^{HH}(\mathbf{r},\mathbf{r}_0,\omega_0)\cdot\mathbf{m}(\omega_0), \tag{4}$$

in which the dyadic tensors $\mathcal{S}^{EH}(\mathbf{r},\mathbf{r}_0,\omega_0)$ and $\mathcal{S}^{HH}(\mathbf{r},\mathbf{r}_0,\omega_0)$ are constructed by identification with Eqs. (1) and (2). For the mixed dyad $\mathcal{S}^{EH}(\mathbf{r},\mathbf{r}_0,\omega_0)$ this identification yields the expression of the nine analytical components,

$$\mathcal{S}^{EH}(\mathbf{r},\mathbf{r}_0,\omega_0) = ik_0\begin{pmatrix} 0 & -\frac{\partial\mathcal{G}_0}{\partial z} & \frac{\partial\mathcal{G}_0}{\partial y} \\ \frac{\partial\mathcal{G}_0}{\partial z} & 0 & -\frac{\partial\mathcal{G}_0}{\partial x} \\ -\frac{\partial\mathcal{G}_0}{\partial y} & \frac{\partial\mathcal{G}_0}{\partial x} & 0 \end{pmatrix}. \tag{5}$$

Equations (1) and (2) define the *so-called* illumination field. Since the materials considered in this article do not directly respond to the optical magnetic field, the coupling with the nanoparticle is entirely described by the first equation. A complete theoretical investigation of this illumination mode requires the accurate computation of the optical field distribution inside the nanostructure for every location $\mathbf{r}_0$ of the magnetic dipole. As discussed in the literature, the recent developments of real-space approaches for electromagnetic scattering and light confinement established powerful tools for the calculation of the electromagnetic response of complex mesoscopic systems to an arbitrary illumination field [35]. Particularly, the technique of the generalized field propagator described in Ref. [34] provides a convenient basis to derive the electromagnetic response of an arbitrary system to a great number of different external excitation fields [42]. Our approach is based on the computation of a unique generalized field propagator $\mathcal{K}(\mathbf{r}',\mathbf{r}'',\omega_0)$ that contains the entire response of the nanostructure to any incident electric field $\mathbf{E}_0(\mathbf{r}'',\omega_0)$. Consequently, the self-consistent electric field $\mathbf{E}(\mathbf{r}_0,\mathbf{r}',\omega_0)$ created inside the nanosystem by a magnetic dipole located at $\mathbf{r}_0$ can be written as

$$\mathbf{E}(\mathbf{r}_0,\mathbf{r}',\omega_0) = \int_v \mathcal{K}(\mathbf{r}',\mathbf{r}'',\omega_0)\cdot\mathbf{E_0}(\mathbf{r}'',\omega_0)d\mathbf{r}'', \tag{6}$$

in which the integral runs over the volume v of the particle. As demonstrated in Ref. [34], the dyadic $\mathcal{K}$ writes

$$\mathcal{K}(\mathbf{r}',\mathbf{r}'',\omega_0) = \mathbf{I}\delta(\mathbf{r}'-\mathbf{r}'') + \mathcal{S}(\mathbf{r}',\mathbf{r}'',\omega_0)\cdot\chi(\mathbf{r}'',\omega_0), \tag{7}$$

where δ is the three-dimensional Dirac function, and $\mathcal{S}(\mathbf{r}',\mathbf{r}'',\omega_0)$ is the optical field-susceptibility tensor of the nanostructure of electric susceptibility $\chi(\mathbf{r}'',\omega_0)$.

Equation (6) gives access to the electric field inside the nanostructure and therefore to the polarization $\mathbf{P}(\mathbf{r}_0,\mathbf{r}'',\omega_0) = \chi(\mathbf{r}'',\omega_0)\cdot\mathbf{E}(\mathbf{r}_0,\mathbf{r}'',\omega_0)$ induced for each position $\mathbf{r}_0$ of the magnetic dipole. The magnetic field generated outside of the

particle can then be calculated by introducing the second mixed-field susceptibility $\mathcal{S}^{HE}(\mathbf{r},\mathbf{r}',\omega_0) = \mathcal{S}^{EH}(\mathbf{r}',\mathbf{r},\omega_0)$ [36],

$$\mathbf{H}(\mathbf{r}_0,\mathbf{r},\omega_0) = \int_v \mathcal{S}^{HE}(\mathbf{r},\mathbf{r}',\omega_0)\cdot\mathbf{P}(\mathbf{r}_0,\mathbf{r}',\omega_0)d\mathbf{r}', \quad (8)$$

which, in a concise form, leads to

$$\mathbf{H}(\mathbf{r}_0,\mathbf{r},\omega_0) = \mathcal{S}_p^{HH}(\mathbf{r},\mathbf{r}_0,\omega_0)\cdot\mathbf{m}(\omega_0), \quad (9)$$

where $\mathcal{S}_p^{HH}(\mathbf{r},\mathbf{r}_0,\omega_0)$ defines the magnetic field susceptibility associated with the nanostructure (p),

$$\mathcal{S}_p^{HH}(\mathbf{r},\mathbf{r}_0,\omega_0) = \int_v d\mathbf{r}' \int_v d\mathbf{r}''\mathcal{S}^{HE}(\mathbf{r},\mathbf{r}',\omega_0) \cdot\chi(\mathbf{r}',\omega_0)\cdot\mathcal{K}(\mathbf{r}',\mathbf{r}'',\omega_0)\cdot\mathcal{S}^{EH}(\mathbf{r}'',\mathbf{r}_0,\omega_0). \quad (10)$$

Here, the center dot "·" signifies the matrix product. This general relationship, derived from the theory of linear response, brings to light the complex link between the electrical response of matter (contained in χ and $\mathcal{K}$) and the magnetic response of vacuum, through the mixed propagators $\mathcal{S}^{EH}$ and $\mathcal{S}^{HE}$. The combination of these response functions shows in a concise way how a nanostructure, which originally does not possess any magnetic response in the optical spectrum, can nevertheless yield a *magnetic-magnetic* response. Equation (10) summarizes with mathematical clarity the back action of the electromagnetic near field on a magnetic quantum emitter via the curl of the electric field, mediated by the presence of a nonmagnetic nanostructure.

III. MAGNETIC DIPOLE DECAY RATE CLOSE TO SMALL DIELECTRIC PARTICLES

Equation (10) allows us to obtain a general expression for the decay rate $\Gamma_m(\mathbf{r}_0,\omega_0)$ associated with a *magnetic dipole transition* of amplitude m_{eg} [13],

$$\Gamma_m(\mathbf{r}_0,\omega_0) = \Gamma_m^0(\omega_0)\left\{1+\frac{3}{2k_0^3}\mathbf{u}\cdot\mathrm{Im}\left[\mathcal{S}_p^{HH}(\mathbf{r}_0,\mathbf{r}_0,\omega_0)\right]\cdot\mathbf{u}\right\}, \quad (11)$$

where $\Gamma_m^0(\omega_0) = 4k_0^3 m_{eg}^2/3\hbar$ represents the natural decay rate of the magnetic transition and $\mathbf{u}$ labels the dipole orientation.

The next objective of this article is to supply a full analytical treatment of $\Gamma_m(\mathbf{r}_0,\omega_0)$. To achieve this goal, we deliberately reduce the physical model to a simple two-level system coupled to a single spherical nanoparticle, as shown in Fig. 2(a). We have chosen to illustrate our method with dielectric materials as they offer an interesting alternative to metals with reduced dissipative losses and large resonant enhancement of both electric and magnetic near fields [43–45].

In this case, a set of simple analytical equations can be derived that include all the physical effects mentioned above. Indeed, we have $\mathcal{K}(\mathbf{r}',\mathbf{r}'',\omega_0) = \mathbf{I}\delta(\mathbf{r}'-\mathbf{r}'')$, $\chi(\mathbf{r}'',\omega_0) = \alpha_e(\omega_0)\delta(\mathbf{r}'')$, where $\alpha_e(\omega_0)$ is the dynamical dipolar polarizability of the sphere, and finally

$$\mathcal{S}_p^{HH}(\mathbf{r},\mathbf{r}_0,\omega_0) = \alpha_e(\omega_0)\mathcal{S}^{HE}(\mathbf{r},0,\omega_0)\cdot\mathcal{S}^{EH}(0,\mathbf{r}_0,\omega_0). \quad (12)$$

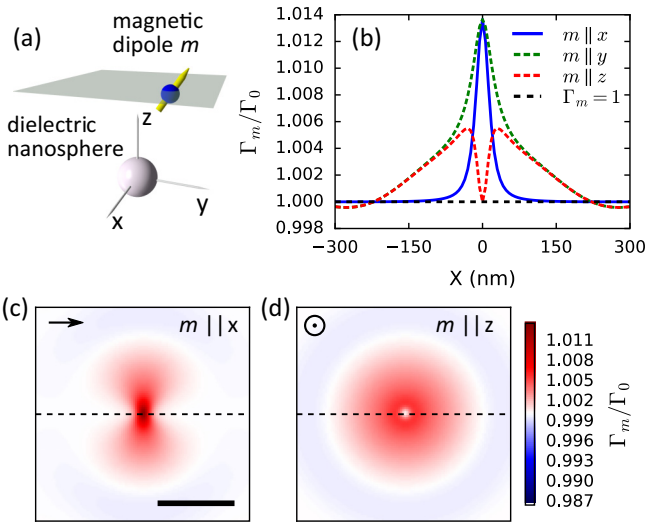

FIG. 2. (a) Single dielectric sphere of polarizability $\alpha_e = 1688$ nm^3 (corresponding to $n = 2$, $r = 15$ nm), raster scanned by a magnetic dipole at constant height $z_0 = 20$ nm. (b) Cross section of $\overline{\Gamma}_m$ computed at $\lambda_0 = 500$ nm for the three orientations u_x, u_y, and u_z of the dipole. (c), (d) Corresponding maps computed in the plane $(x_0, y_0, z_0 = 20$ nm). The maps have been computed from the complete expression of Eq. (13). Maps are 600×600 nm^2, and the scale bar is 200 nm.

This relation can be further simplified by replacing both $\mathcal{S}^{EH}$ and $\mathcal{S}^{HE}$ by their analytical expressions. In a plane defined by $x_0 = 0$, i.e., $\mathbf{r}_0 = (0, y_0, z_0)$, we get the following simple expression when $\mathbf{r} = \mathbf{r}_0$ [cf. Eq. (11)],

$$\mathcal{S}_p^{HH}(\mathbf{r}_0,\mathbf{r}_0,\omega_0) = \alpha_e(\omega_0)\mathcal{A}e^{2ik_0r_0}\left\{-\frac{k_0^4}{r_0^4}-\frac{2ik_0^3}{r_0^5}+\frac{k_0^2}{r_0^6}\right\}, \quad (13)$$

where $r_0 = |\mathbf{r}_0|$ and the matrix $\mathcal{A}$ is defined by

$$\mathcal{A} = \begin{pmatrix} y_0^2+z_0^2 & 0 & 0 \\ 0 & z_0^2 & -y_0z_0 \\ 0 & -y_0z_0 & y_0^2 \end{pmatrix}. \quad (14)$$

In consequence, $\mathcal{S}_p^{HH}$ has the dimension of an inverse volume.[1] A concise expression of the normalized magnetic decay rate $\overline{\Gamma}_m = \Gamma_m/\Gamma_m^0$ can then be deduced by replacing this relation into (11),

$$\overline{\Gamma}_m(\mathbf{r}_0,\omega_0) = 1+\alpha_e(\omega_0)\mathbf{u}\cdot\mathcal{A}\cdot\mathbf{u} \times\left\{\sin(2k_0r_0)\left(-\frac{3k_0}{2r_0^4}+\frac{3}{2k_0r_0^6}\right) -\cos(2k_0r_0)\frac{3}{r_0^5}\right\}, \quad (15)$$

in which the polarizability dissipation term $\mathrm{Im}\,\alpha_e(\omega_0)$ has been neglected. We set $x_0 = 0$ to obtain the simplest equations

[1] α_e has a dimension of r^3, $\mathcal{A}$ of r^2, and all terms in the curly brackets of Eq. (13) are homogeneous to r^{-8}.

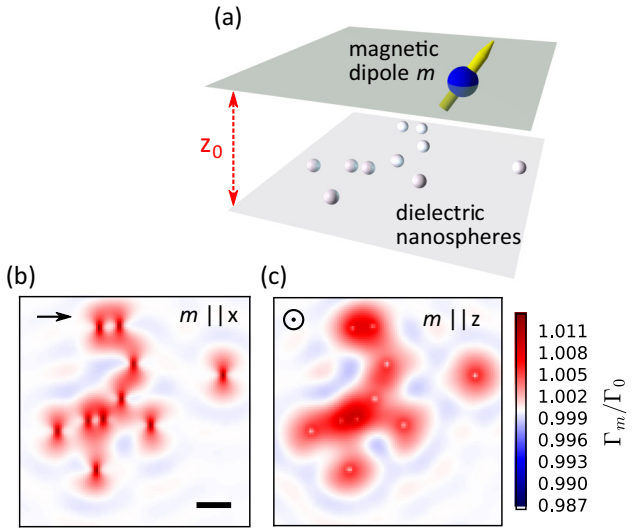

FIG. 3. (a) Random distribution of dielectric spheres of polarizability $\alpha_e = 1688$ nm^3 (corresponding to $n = 2$, $r = 15$ nm), raster scanned by a magnetic dipole at constant height $z_0 = 20$ nm. (b) and (c) show normalized decay maps for u_x and u_z orientation of the magnetic dipole, respectively. Computed with $\lambda_0 = 500$ nm. Maps are 1600×1600 nm^2, and the scale bar is 200 nm.

possible. Adding it as a free parameter is straightforward, yet renders Eqs. (14) and (15) more complex. The case of a single dipolar dielectric sphere presented in Fig. 2 shows that the contrast patterns are extremely sensitive to the dipole orientation. The contrast is generally positive on top of the particle except when the dipole is aligned perpendicularly to the scanning plane (x_0, y_0), in which case it vanishes, the sphere becoming invisible for the magnetic dipole. Such a peculiar behavior explicitly appears in Eqs. (14) and (15) for small interaction distances, in particular, when the magnetic dipole enters the very subwavelength range corresponding to $2k_0 r_0 \ll 1$.

As a second example, we consider in Fig. 3 a set of p identical dielectric particles deposited on a transparent substrate positioned at random locations $\mathbf{r}_i$ ($i = 1$ to p). The optical properties of such a system can be described by first inserting the relation

$$\chi(\mathbf{r},\omega_0) = \alpha_e(\omega_0) \sum_{i=1}^{p} \delta(\mathbf{r} - \mathbf{r}_i) \tag{16}$$

in Eq. (10) and then in expression (11). The results are presented in Figs. 3(b) and 3(c). When the particles are well separated from each other, typically by one wavelength or more, they display a contrast similar to the one described in Fig. 2. This contrast is reinforced when several particles are grouped together. Isolated particles and assemblies of particles are surrounded by pseudoperiodic ripples that reveal the interferences between the emitting magnetic dipole and the sample.

IV. ELECTRIC AND MAGNETIC DIPOLE DECAY RATE CLOSE TO COMPLEX DIELECTRIC NANOSTRUCTURES

Whereas Eqs. (10) and (11) provide analytical expressions of the decay rate of magnetic dipoles placed close to very simple nano-objects, these equations can be complemented by an adequate discretization of the particle volume to describe light emission from dipoles in the vicinity of nanostructures of arbitrary geometries. To this end, we numerically implement the complete computation of the generalized propagator $\mathcal{K}(\mathbf{r}',\mathbf{r}'',\omega_0)$ as described in Ref. [34], together with $\chi(\mathbf{r},\omega_0) = [\epsilon(\omega_0) - \epsilon_{\text{env}}]/4\pi$ (cgs units), where ϵ_{env} defines the permittivity of the environment. We then use the propagator $\mathcal{K}$ associated with the nanostructure with the mixed-field susceptibilities $\mathcal{S}^{HE}$ and $\mathcal{S}^{EH}$ in a discretized version of Eq. (10),

$$\mathcal{S}_p^{HH}(\mathbf{r},\mathbf{r}_0,\omega_0) = \sum_{i=1}^{N} V_{\text{cell}} \sum_{j=1}^{N} V_{\text{cell}} \mathcal{S}^{HE}(\mathbf{r},\mathbf{r}_i,\omega_0) \cdot \chi(\mathbf{r}_i,\omega_0) \cdot \mathcal{K}(\mathbf{r}_i,\mathbf{r}_j,\omega_0) \cdot \mathcal{S}^{EH}(\mathbf{r}_j,\mathbf{r}_0,\omega_0). \tag{17}$$

The sums (indexes i and j) run over all N discretization cells (of volume V_{cell}) forming the nanostructure. This numerical procedure gives access to the optical response of complex systems, such as the ones described in Fig. 4. In this example, we have applied this technique to visualize the footprint induced by a perfect square corral composed of 20 dielectric structures in the initially flat ED and MD decay-rate maps. The extension of the entire nanostructure is 1.1 μm, and the refractive index is $n_{\text{pad}} = 2$. A modification of the decay rates ranging between 20% and 50% is obtained when the magnetic dipole is 30 nm above the nanostructures [Figs. 4(c) and 4(d)]. Although the coupling is more efficient with an electric dipole [Figs. 4(a) and 4(b)], especially when it is perpendicular, the coupling of the magnetic dipole with the dielectric structure remains quite significant and could be easily observed. In particular, the normalized contrast $\overline{\Gamma}_m - 1$ will be further enhanced when increasing n_{pad} from 2 to 4 or 5 using high optical index dielectric or semiconductor materials (TiO_2, Si, or even Ge). To demonstrate this enhancement, we show in Figs. 4(e)–4(h) a flat silicon structure $n \approx 4.3$ forming the letters "Si," on which a magnetic decay-rate enhancement of more than a factor 5 can be observed. Moreover, we notice that the maps of the ED and MD decay rates display very specific features that will allow one to discriminate unambiguously the *electric* or *magnetic* nature of the atomic transition. A similar identification method has been proposed and demonstrated using back-focal plane imaging of electric/magnetic dipole luminescence from rare-earth-doped films [46,47]. Our results suggest an alternative discrimination technique using nanostructured substrates, which could be performed on less complex optical detection schemes.

For instance, when the emitting dipole is oriented along the (OX) axis [maps shown in Figs. 4(a), 4(c) 4(e), and 4(g)], we observe a contrast reversal above the dielectric pads when passing from an *electric* to a *magnetic* dipole. This striking phenomenon is accompanied by a shift of the fringe pattern inside the corral by half a wavelength. Finally, another type of contrast change is observed when the dipole is perpendicular

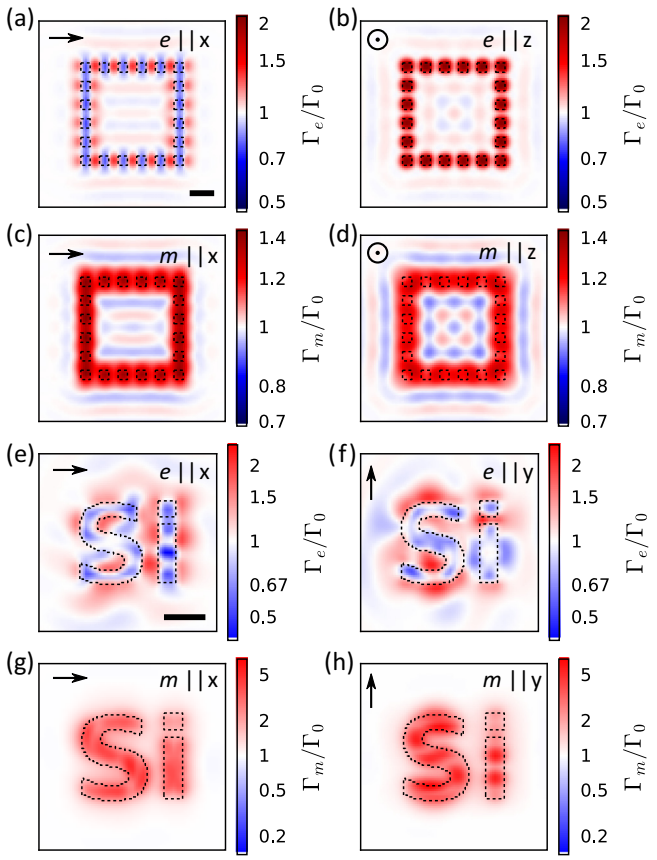

FIG. 4. (a)–(d) Maps of the decay rates of electric (ED) and magnetic dipoles (MD) 30 nm above a square corral of 20 dielectric nanocubes. The spacing between each cube of dimensions $100 \times 100 \times 100$ nm^3 is 100 nm and the optical index is $n = 2.0$. The maps (a)–(d) have a size of 2×2 μm^2. (a) ED oriented along the OX axis; (b) ED oriented along the OZ axis; (c) and (d) same computation for a MD. (e)–(h) Maps of the (e), (f) ED and (g), (h) MD decay rate 30 nm above a silicon nanostructure ($n = 4.3$) composing the letters "Si" (structure height $H = 50$ nm). The maps (e)–(h) are 1×1 μm^2 large. (e) ED along OX; (f) ED along OY; (g) and (h) same for a MD. A logarithmic color scale is used due to the larger contrast in the decay rates. All maps are computed at $\lambda_0 = 500$ nm. Dashed black lines indicated the contours of the nanostructures. Scale bars are 200 nm.

to the sample. In this second case, as illustrated by the maps shown in Figs. 4(b) and 4(d), we move from a highly localized signal around the pads [map in Fig. 4(b)] to a broader response distributed along the corral rows [map in Fig. 4(d)].

V. EVOLUTIONARY OPTIMIZATION OF METAL NANOSTRUCTURES FOR MAXIMUM MAGNETIC DECAY RATE

In order to demonstrate the versatility of our model, we couple our numerical framework to an evolutionary optimization (EO) algorithm. EO tries to find optimum solutions to complex problems by mimicking the process of natural selection. Its principal idea is briefly depicted in Fig. 5(a). Our approach to couple EO to numerical simulations is described in more detail in Ref. [48]. For technical information on the implementation and the used algorithm parameters, see the Supplemental Material (SM) [49]. In the SM, we also show an additional single- as well as a multiobjective evolutionary optimization problem, based on the decay-rate formalism. In this section, we use the permittivity of gold [50] to demonstrate that our formalism is not limited to dielectric materials. The optimization goal is to find a gold nanostructure which maximizes the ratio of magnetic over electric decay rate Γ_m/Γ_e at a fixed location [$\mathbf{r}_0 = (0,0,80)$ nm]. This is a particularly tricky scenario, because metals are known to have a far stronger response to electric dipole transitions than to magnetic ones. We use the evolutionary algorithm to optimize the geometry of a planar structure composed of 100 gold pillars (each $20 \times 20 \times 60$ nm^3), lying on a plane of 1000×1000 nm^2 [see Fig. 5(b)]. We recall here that each subwavelength pillar does not support a direct magnetic response on its own. To render the positioning easier, the possible locations on the plane lie on a discretized grid (steps of 20 nm). The structure is placed in vacuum and the wavelength is fixed at $\lambda = 500$ nm. We evolve a population of 150 individuals (nanostructures) over 2500 generations. Each of the individuals is a parameter set consisting of positions for the 100 gold pillars, hence describing one possible structure. We tested the convergence by running the same optimization several times, reproducibly yielding similar structures and values for the decay-rate ratio.

The optimum structure found by the EO algorithm is shown in Fig. 5(c). Mappings of the decay-rate ratio as well as the electric and magnetic decay rates are shown in Figs. 5(d)–5(g). Obviously, the algorithm succeeded in finding a gold nanostructure which significantly promotes magnetic decay at the target position [see Fig. 5(d)]. This is particularly remarkable, because although gold structures easily provide very strong electric dipole decay-rate enhancements, the magnetic LDOS is known to be usually very weak in metallic nanoparticles [26].

Two effects are being exploited by the optimized structure: The first mechanism is the different confinement of the decay rates for electric and magnetic dipoles close to the material. The electric decay-rate enhancement in the proximity of the gold pillars is high, but confined to a very small volume around the material. The magnetic decay rate, on the other hand, is more loosely enhanced around the gold clusters, leading to regions in their vicinity where Γ_e is almost not affected, while Γ_m still shows significant enhancement [cf. Figs. 5(e) and 5(f)]. The second effect is a modulation of the decay rate inside a larger resonator due to interference, similar to the corral shown in Figs. 1 and 4. At $\lambda = 500$ nm, the above presented corral had a maximum of Γ_e in its center [see Figs. 4(b) and 4(d)]. In contrast to this, the evolutionary algorithm distributed a fraction of the material (outer, circular structure) such that Γ_m is maximum in its center, which can be seen in Fig. 5(g), where the decay rate has been calculated for the isolated outer structure.

We will conclude this section with some considerations on the convergence. One might wonder why the structure does not consist of perfect circles—this would very likely result in even better performance. Concerning this question, we have to keep in mind that $(51 \times 51)!/(51 \times 51 - 100)! \approx 10^{341}$ possibilities exist to distribute the 100 gold pillars on the available positions on the plane. Yet, the evolutionary algorithm did

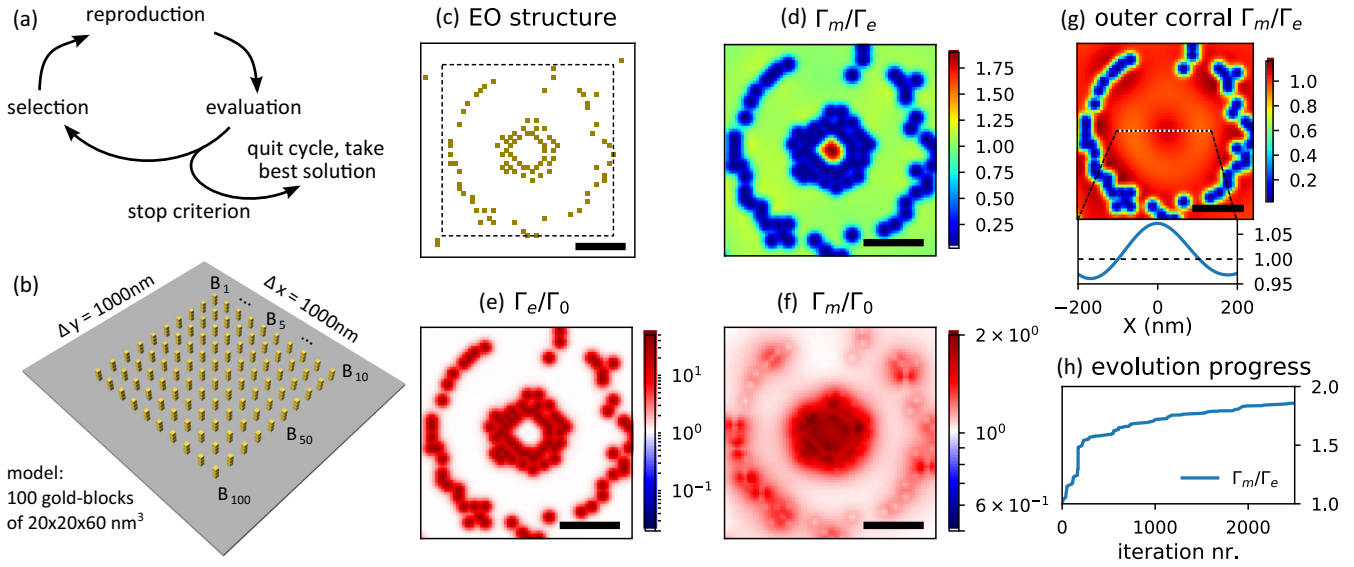

FIG. 5. (a) Evolutionary optimization cycle. (b) Sketch of the structure model for optimization: Free parameters are the positions of 100 gold blocks (B_i) on the XY plane (in vacuum). (c) Gold structure for optimum Γ_m/Γ_e contrast at the center [$\mathbf{r}_0 = (0,0,80)$ nm], found by EO. (d)–(g) Decay-rate analysis of the EO solution. (d) Mapping of the ratio of magnetic and electric decay rate 20 nm above the structure. (e), (f) Relative electric and magnetic decay rates above the structure, respectively. (g) Ratio of magnetic and electric decay rate for only the outer part of the structure, also leading to an enhancement of Γ_m at the target location. At the bottom of (g), Γ_m/Γ_e is shown along a profile in the center of the map. (h) Progress of the evolutionary algorithm. A logarithmic color scale is used for the maps (e) and (f). All results are computed at $\lambda_0 = 500$ nm and for a dipole orientation along OZ. Scale bars are 200 nm. Mapping (c) is 1000×1000 nm^2, and (d)–(g) are 800×800 nm^2 large [area indicated by a dashed square in (c)].

only evaluate $2500 \times 150 < 4 \times 10^5$ different arrangements. Therefore, the reason why the material is not distributed on perfect circles is the heuristic nature of the evolutionary optimization algorithm. The search for the best structure did simply not converge to the very optimum. Comparing the optimized structure to an idealized version reveals that the possible improvement in Γ_m/Γ_e is only in the order of $\approx 1\%$ (see also SM). We conclude that, despite the residual disorder in the geometry, the EO algorithm did converge very close to the ideal structure. Hence, EO is a promising approach to this kind of problem.

VI. CONCLUSIONS AND PERSPECTIVES

In summary, we have developed a concise theoretical framework to describe the dynamics of light emission from magnetic dipoles located in complex nanostructured environments. This method, based on mixed-field susceptibilities, provides analytical expressions of the decay rate in the case of very simple environments. When the magnetic dipole is located close to nanostructures of arbitrary geometries, the computation of the MD decay rate involves the discretization of the nanostructure volume, the computation of a generalized propagator, and finally the computation the decay rate from mixed-field susceptibilities. This versatile framework is well suited to describe the emission of light from emitters involving both electric and magnetic dipole transitions as well as nano-optical processes comprising confined electric and magnetic fields. In addition, our framework is very flexible and can easily be extended. For instance, nonlocality effects might be included by following the descriptions of Ref. [51]. Owing to its computational simplicity, the method can also be employed within more complex numerical schemes. We demonstrated this possibility by coupling the magnetic decay-rate calculation to an evolutionary optimization algorithm, which we employed to design a gold nanostructure for maximum contrast between magnetic and electric EM-LDOS. We also applied our method to the decay rate close to complex dielectric nanostructures. Our results suggest that it could be possible to identify the nature of the transition involved in the emission process (ED vs MD) from the variations of the decay rate in the vicinity of nanostructures. Finally, nanostructures possessing a particularly high contrast regarding dipole orientations could be designed using our evolutionary optimization.

ACKNOWLEDGMENTS

We thank C. Majorel for his very useful contributions in the context of a Master's training. This work was supported by Programme Investissements d'Avenir under Program No. ANR-11-IDEX-0002-02, Reference No. ANR-10-LABX-0037-NEXT, and by the computing facility center CALMIP of the University of Toulouse under Grant No. P12167.

[1] L. Novotny and B. Hecht, *Principles of Nano-Optics* (Cambridge University Press, Cambridge, UK, 2006).

[2] P. Anger, P. Bharadwaj, and L. Novotny, Phys. Rev. Lett. **96**, 113002 (2006).

[3] S. Kühn, U. Håkanson, L. Rogobete, and V. Sandoghdar, Phys. Rev. Lett. **97**, 017402 (2006).

[4] A. Kinkhabwala, Z. Yu, S. Fan, Y. Avlasevich, K. Müllen, and W. E. Moerner, Nat. Photonics **3**, 654 (2009).

[5] A. G. Curto, G. Volpe, T. H. Taminiau, M. P. Kreuzer, R. Quidant, and N. F. van Hulst, Science **329**, 930 (2010).

[6] P. Biagioni, J.-S. Huang, and B. Hecht, Rep. Prog. Phys. **75**, 024402 (2012).

[7] L. Novotny and N. van Hulst, Nat. Photonics **5**, 83 (2011).

[8] V. V. Klimov, M. Ducloy, and V. S. Letokhov, J. Mod. Opt. **43**, 2251 (1996).

[9] H. Giessen and R. Vogelgesang, Science **326**, 529 (2009).

[10] L. Aigouy, A. Cazé, P. Gredin, M. Mortier, and R. Carminati, Phys. Rev. Lett. **113**, 076101 (2014).

[11] B. Choi, M. Iwanaga, Y. Sugimoto, K. Sakoda, and H. T. Miyazaki, Nano Lett. **16**, 5191 (2016).

[12] S. Karaveli and R. Zia, Phys. Rev. Lett. **106**, 193004 (2011).

[13] R. Carminati, A. Cazé, D. Cao, F. Peragut, V. Krachmalnicoff, R. Pierrat, and Y. De Wilde, Surf. Sci. Rep. **70**, 1 (2015).

[14] D. G. Baranov, R. S. Savelev, S. V. Li, A. E. Krasnok, and A. Alù, Laser Photonics Rev. **11**, 1600268 (2017).

[15] A. Cuche, M. Berthel, U. Kumar, G. Colas des Francs, S. Huant, E. Dujardin, C. Girard, and A. Drezet, Phys. Rev. B **95**, 121402(R) (2017).

[16] E. M. Purcell, H. C. Torrey, and R. V. Pound, Phys. Rev. **69**, 37 (1946).

[17] C. Chicanne, T. David, R. Quidant, J. C. Weeber, Y. Lacroute, E. Bourillot, A. Dereux, G. Colas des Francs, and C. Girard, Phys. Rev. Lett. **88**, 097402 (2002).

[18] B. Rolly, B. Bebey, S. Bidault, B. Stout, and N. Bonod, Phys. Rev. B **85**, 245432 (2012).

[19] D. N. Chigrin, D. Kumar, D. Cuma, and G. von Plessen, ACS Photonics **3**, 27 (2016).

[20] H. Chew, Phys. Rev. A **19**, 2137 (1979).

[21] V. V. Klimov and V. S. Letokhov, Laser Phys. **15**, 61 (2005).

[22] M. K. Schmidt, R. Esteban, J. J. Sáenz, I. Suárez-Lacalle, S. Mackowski, and J. Aizpurua, Opt. Express **20**, 13636 (2012).

[23] B. Stout, A. Devilez, B. Rolly, and N. Bonod, J. Opt. Soc. Am. B **28**, 1213 (2011).

[24] T. Feng, Y. Zhou, D. Liu, and J. Li, Opt. Lett. **36**, 2369 (2011).

[25] S. M. Hein and H. Giessen, Phys. Rev. Lett. **111**, 026803 (2013).

[26] P. Albella, M. A. Poyli, M. K. Schmidt, S. A. Maier, F. Moreno, J. J. Sáenz, and J. Aizpurua, J. Phys. Chem. C **117**, 13573 (2013).

[27] M. Mivelle, T. Grosjean, G. W. Burr, U. C. Fischer, and M. F. Garcia-Parajo, ACS Photonics **2**, 1071 (2015).

[28] T. Feng, Y. Xu, Z. Liang, and W. Zhang, Opt. Lett. **41**, 5011 (2016).

[29] M. Burresi, D. van Oosten, T. Kampfrath, H. Schoenmaker, R. Heideman, A. Leinse, and L. Kuipers, Science **326**, 550 (2009).

[30] E. Devaux, A. Dereux, E. Bourillot, J.-C. Weeber, Y. Lacroute, J.-P. Goudonnet, and C. Girard, Appl. Surf. Sci. **164**, 124 (2000).

[31] E. Devaux, A. Dereux, E. Bourillot, J.-C. Weeber, Y. Lacroute, J.-P. Goudonnet, and C. Girard, Phys. Rev. B **62**, 10504 (2000).

[32] C. Girard, J.-C. Weeber, A. Dereux, O. J. F. Martin, and J.-P. Goudonnet, Phys. Rev. B **55**, 16487 (1997).

[33] U. Schröter, Eur. Phys. J. B **33**, 297 (2003).

[34] O. J. F. Martin, C. Girard, and A. Dereux, Phys. Rev. Lett. **74**, 526 (1995).

[35] C. Girard, Rep. Prog. Phys. **68**, 1883 (2005).

[36] G. S. Agarwal, Phys. Rev. A **11**, 230 (1975).

[37] I. Sersic, C. Tuambilangana, T. Kampfrath, and A. F. Koenderink, Phys. Rev. B **83**, 245102 (2011).

[38] A. Kwadrin and A. F. Koenderink, Phys. Rev. B **87**, 125123 (2013).

[39] P. Lunnemann and A. F. Koenderink, Sci. Rep. **6**, 20655 (2016).

[40] J. B. Pendry, Phys. Rev. Lett. **85**, 3966 (2000).

[41] C. M. Soukoulis, S. Linden, and M. Wegener, Science **315**, 47 (2007).

[42] A. Arbouet, A. Mlayah, C. Girard, and G. Colas des Francs, New J. Phys. **16**, 113012 (2014).

[43] R. M. Bakker, D. Permyakov, Y. F. Yu, D. Markovich, R. Paniagua-Domínguez, L. Gonzaga, A. Samusev, Y. Kivshar, B. Luk'yanchuk, and A. I. Kuznetsov, Nano Lett. **15**, 2137 (2015).

[44] M. Decker and I. Staude, J. Opt. **18**, 103001 (2016).

[45] A. I. Kuznetsov, A. E. Miroshnichenko, M. L. Brongersma, Y. S. Kivshar, and B. Luk'yanchuk, Science **354**, aag2472 (2016).

[46] T. H. Taminiau, S. Karaveli, N. F. van Hulst, and R. Zia, Nat. Commun. **3**, 979 (2012).

[47] D. Li, M. Jiang, S. Cueff, C. M. Dodson, S. Karaveli, and R. Zia, Phys. Rev. B **89**, 161409 (2014).

[48] P. R. Wiecha, A. Arbouet, C. Girard, A. Lecestre, G. Larrieu, and V. Paillard, Nat. Nanotechnol. **12**, 163 (2017).

[49] See Supplemental Material at http://link.aps.org/supplemental/10.1103/PhysRevB.97.085411 for a comparison of the analytical and numerical model, additional simulations and technical details, as well as additional examples on the evolutionary optimization.

[50] P. B. Johnson and R. W. Christy, Phys. Rev. B **6**, 4370 (1972).

[51] C. Girard, A. Cuche, E. Dujardin, A. Arbouet, and A. Mlayah, Opt. Lett. **40**, 2116 (2015).